Solar Phys (2007) 245: 191–206
DOI 10.1007/s11207-007-9019-1

The Latitudinal Effect of Corotating Interaction Regions on Galactic Cosmic Rays

A.P. Rouillard · M. Lockwood

Received: 24 April 2007 / Accepted: 31 July 2007 / Published online: 27 September 2007

Abstract The response of galactic cosmic rays (GCRs) to an isolated enhancement of the non-axisymmetric component of the solar open magnetic field between June and November 1996 is investigated by using a combination of solar observations and numerical modelling of the interplanetary medium. The most obvious coronal hole visible from Earth at the time had little shielding effect on the flux of GCRs, as measured at Earth by neutron monitors. It is found that the evolution of the corotating interaction regions generated by a less obvious coronal hole was the principal controlling factor. Moreover, we demonstrate the imprint of the latitudinal and longitudinal evolution of that coronal hole on the variation of GCRs. The latitudinal extent of this solar minimum corotating interaction region had a determining, but local, shielding effect on GCRs, confirming previous modelling results.

Keywords Sun: magnetic field · Sun: corotating interaction regions · Interplanetary medium: galactic cosmic rays

1. Introduction

Galactic cosmic rays (GCRs) gyrating along open solar magnetic field lines are scattered by irregularities on these field lines with scale length comparable to the GCR gyroradius. This scattering inhibits GCRs from moving towards the inner heliosphere by forcing a random-walk or slow diffusion process. Additional modulation mechanisms are the advective effect of the supersonic solar wind, which carries the frozen-in magnetic field, the adiabatic cooling effect of the radial expansion of the wind, and the coherent influence of large-scale field gradient and curvature "drift" effects.

A.P. Rouillard (✉) · M. Lockwood
Space Physics Division, Space Science and Technology Department, Rutherford Appleton Laboratory, Chilton, Oxfordshire OX11 0QX, UK
e-mail: alexisrouillard@yahoo.co.uk

A.P. Rouillard · M. Lockwood
Space Environment Physics Group, School of Physics and Astronomy, University of Southampton, Southampton SO17 1BJ, UK

Observational studies have recently shown that the flux of GCRs could be largely regulated by the evolution of the footprint location of open solar magnetic field lines (Cliver and Ling, 2001; Wang, Sheeley, and Rouillard, 2006; Rouillard, 2007). From our understanding of the solar corona and the evolution of open magnetic flux on the Sun (Wang, Hawley, and Sheeley, 1996; Fisk and Schwadron, 2001) it was suggested that the occurrence of isolated coronal holes (CHs), where these field lines are rooted during solar maximum, could be a controlling factor for shielding the inner heliosphere from GCRs (Wang, Sheeley, and Rouillard, 2006; Rouillard, 2007). These coronal holes give fast solar wind outflow and hence control the formation of corotating interaction regions (CIRs) at the interface of the fast streams and the slow solar wind. The evolution of CIRs is reasonably well understood following intensive analytical (Lee, 2001) and numerical work (Pizzo and Gosling, 1994). Their relevance to GCR shielding has been demonstrated observationally (Heber and Burger, 1999) and theoretically (Kóta and Jokipii, 1991; Kóta, 1999, and references therein). The shock waves and compression regions (in which the interplanetary magnetic field is enhanced) ahead of CIRs are thought to be the main source of GCR modulation (Kóta, 1999). In the case of a single CIR, modulation models predict a rather limited effect and this is confirmed by observations of GCR decreases at Earth of only a few percent following transient passages of isolated CIRs. GCRs are thought to recover between two successive CIRs, in particular in the rarefied fast-flow regions behind the turbulent leading edge: The faster wind speed results in straighter field lines, which are likely to contain fewer fluctuations able to scatter GeV particles. The variation in the solar wind speed is substantially smaller than that in the magnetic field (which can change by an order of magnitude) so that diffusion effects from scattering by field irregularities are thought to predominate (Kóta, 1999). Particle drifts will be reduced by the enhanced turbulence within the CIRs but will be faster in the weak field between CIRs. Drift streamlines largely flow around CIRs; thus the global effect of an individual CIR remains limited beyond the region of compressed interplanetary magnetic field (IMF).

The study of solar-minimum GCR modulation produced by single CIRs is easier to carry out and provides very useful information for studying the propagation of energetic charged particles through the heliosphere, which is fundamental to gaining understanding of the 11-year modulation. We here present observations on the evolution of GCRs during the second half of the year 1996 near solar minimum when simultaneous observations were made of the solar photosphere and corona by the *Solar and Heliospheric Observatory* (SOHO) spacecraft, of the interplanetary medium at 1 AU by a combination of satellites (intercalibrated by the OMNI team), and of the flux of GCRs at Earth by a network of neutron monitors. Most studies of CIR/CME effects on galactic cosmic rays have compared GCR variations to solar wind speed features in the ecliptic (Morfill, Richter, and Scholer, 1979) and have not directly considered the latitudinal dimension of CIR/CME.

Firstly, we show that SOHO coronal images and solar magnetograms help provide a clear picture of the state of the solar corona between Carrington rotations (CRs) 1912 to 1918. Secondly, we show that the most obvious coronal feature seen from Earth at that time is not responsible for the observed recurring galactic cosmic ray decreases. Thirdly, we use numerical modelling of the inner ($<2.5\,R_s$) and outer corona ($>2.5\,R_s$) to investigate the role of the morphology of CIRs on GCR shielding during this period. Using these three parts, we investigate the consequence of an isolated increase in the open solar flux with low-latitude footprints on GCRs.

2. Solar Minimum Activity and Coronal Hole Extensions

The largest active region of a photospheric activity nest that lasted from May to November 1996 emerged in July (NOAA 7978) at latitude $\psi = -10°$ and Carrington longitude $\phi = 259°$, while the Sun was near its minimum activity. This active region (identified subsequently as NOAA 07981 and NOAA 07986 in CRs 1912 and 1913, respectively) triggered the formation of extensions of both the northern and southern polar coronal holes. Wang *et al.* (1997a) described the evolution of the photospheric and lower coronal field from CRs 1908 (starting 4 March) to 1913 (starting 22 August) using a potential field source surface (PFSS) extrapolation of the photospheric flux recorded by solar magnetographs. Wang *et al.* showed that the emergence of photospheric field during CR 1911 led to the enhancement of the original field distribution and its associated equatorial dipole field, which led to the widening of the streamer belt. The associated enhancement of the flux of open magnetic field lines located at low latitudes (<45°) is shown in Figure 1b. This low-latitude open flux was quantified by using the PFSS method and consists of open field line footprints, which have no symmetric distribution relative to the solar rotation axis and are therefore part of the non-axisymmetric field (Wang, Sheeley, and Rouillard, 2006). Associated with this event, a series of large recurrent decreases were seen in the flux of GCRs, measured by neutron monitors around the globe (Bromage, Browning, and Clegg, 2001). The data from the Climax neutron monitor are plotted in Figure 1a. Bromage, Browning, and Clegg showed that this recurrent variation occurred while there was a large extension of the northern polar CH, triggered by the emergence of the active region. Moreover, they showed that the source of the main recurrent GCR decrease could not have been forced by this northern polar coronal hole extension; rather, it was forced by probable turbulence in the streamer belt. Their analysis is re-examined here and carried further.

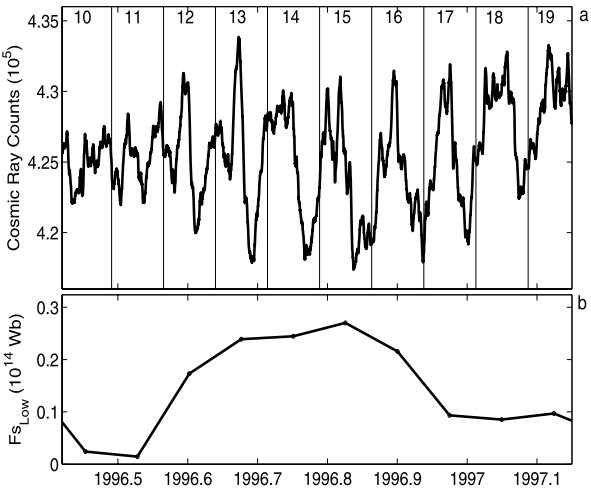

Figure 1 (a) The 24-hour running means of GCR counts recorded by the Climax neutron monitor (GCR rigidity, $R_C > 3$ GV). The Carrington rotation numbers (minus 1900) are indicated together with vertical bars giving their start and end dates. The recurrent variation is clearly visible and is enhanced from CR 1912/CR 1913 onwards. (b) The variations predicted by PFSS of the open solar flux with low-latitude (<45°) field line footprints, $F_s|_{Low}$. Only one value of $F_s|_{Low}$ can be obtained per CR.

3. Coronal Activity Compared to 1 AU Speed Enhancements

The recurrent decreases in cosmic rays are plotted in Figure 2, which shows the Climax neutron monitor counts as a function of CR number and Carrington longitude. Carrington longitude decreases in the course of a solar rotation and hence time flows from top to bottom and from left to right on the plot. The Carrington longitude, ϕ_1, is for a heliocentric distance $r = 1$ AU. This format was adopted to reveal the large recurrent decrease (red to blue), starting at around longitude $\phi_1 \approx 180°$. Figure 3 shows a series of synoptic maps derived from images taken by the Extreme Ultraviolet (EUV) Imaging Telescope (EIT) in the Fe line (195 Å) onboard SOHO for CR 1912 to CR 1917. These images give values of the line intensity detected around the central meridian and were compiled by Benevolenskaya, Kosovichev, and Scherrer (2001). The original 1024×1024 pixel images were binned to 512×512 pixels, and then each pixel of the CCD rectangular coordinates was transformed into the Carrington coordinate system. In this case the Carrington longitude (ϕ_0) is at the coronal source surface, assumed to be at $r = 2.5R_\odot$. For days when there were no data, Benevolenskaya, Kosovichev, and Scherrer used a wider longitudinal stripe from the previous image to cover the missing values. The resolution of these maps is 1° degree in both longitude from 0° to 360° and latitude ψ from −83° to 83°.

On these images the black areas correspond to cool regions of the solar corona where opened field lines allow plasma to stream out continuously and hence they are images of coronal holes. The bright regions are hot regions where sunspots have emerged on the underlying photosphere. Coronal holes can also be identified in the NSO/Kitt Peak He I 10830 Å synoptic maps. We have plotted in red and on top of the EIT synoptic maps the estimates of polar coronal hole location made at NSO (Harvey and Recely, 2002). These observations

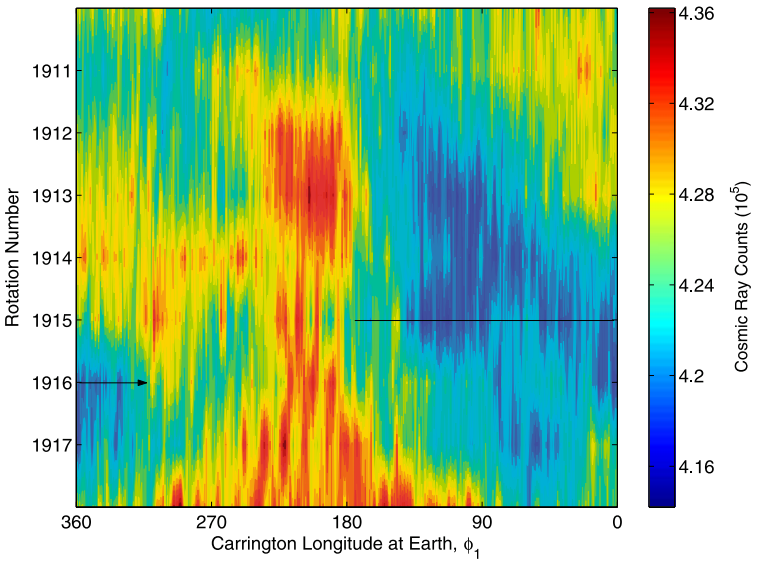

Figure 2 Each vertical band shown in Figure 1a is here re-plotted in a Carrington rotation number versus Carrington longitude format. This format will be useful in the discussion of the state of the corona in the next figures. The largest and longest lived decrease in GCR first appears during CR 1912 at Carrington longitude 180° and reaches its maximum extent in CR 1915, extending into rotation 1916, as indicated by a long black arrow.

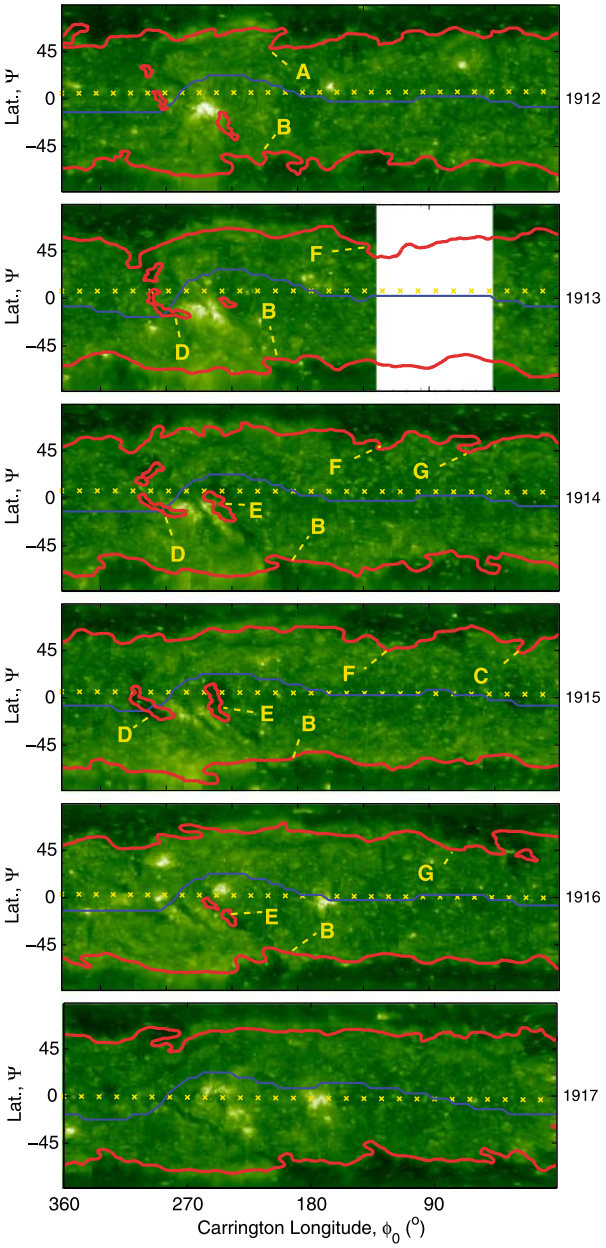

Figure 3 EIT synoptic maps constructed by Benevolenskaya, Kosovichev, and Scherrer (2001) for CR numbers given to the right of each panel. The boundaries of coronal holes estimated by Harvey and Recely (2002) using NSO/Kitt peak He I 10830 Å synoptic maps are shown as thick red lines. The latitudinal excursions of the HCS from PFFS analysis of WSO magnetograms are shown as a blue line. The locations of various low-latitude CHs and extensions of polar coronal holes are identified and labelled (A to G). These synoptic maps have been flipped (east and west have been reversed) so that time flows from left to right.

provide an independent means of localising CHs in these rotations. The plots shown here are in latitude ψ versus time t format with time again expressed in Carrington longitude ϕ_0, so that each panel covers a full solar rotation. These synoptic maps have been flipped (east and west have been reversed) so that time flows from left to right. The position of the Heliospheric Current Sheet (HCS) obtained by application of a PFFS extrapolation of the corresponding Wilcox Solar Observatory (WSO) magnetograms are indicated by a blue curve. We note that although the assembled EIT images have a 1° resolution, the magnetograms

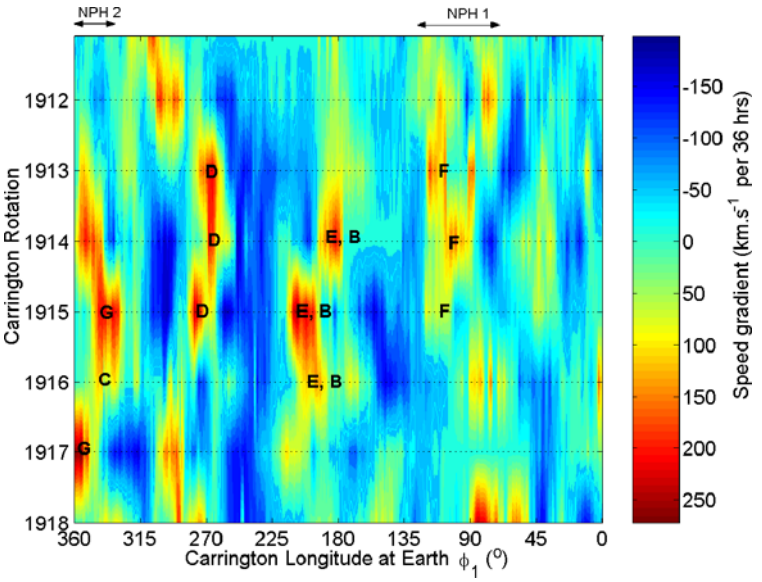

Figure 4 The speed gradients ΔV at Earth, evaluated from in situ, near-Earth solar wind speed data obtained by the IMP 8 satellite and plotted as a function of CR number and longitude ϕ_1. Because of the 4 – 5 day transit times, features appear at longitudes 40° – 50° lower than in Figure 3. The gradients are evaluated by taking solar wind speeds separated by 36 hours. The influence of identified CHs in Figure 3 are indicated by the corresponding letters.

used to generate the PFSS extrapolations have a 2° – 5° resolution, a factor considered later. The radially projected orbit of the Earth is indicated by yellow crosses: for these rotations the Earth is mostly located north of the solar ecliptic plane. These plots show typical solar minimum conditions with two well-formed polar CHs. The emergence of the active region (bright feature at $\phi_0 = 255°$) has led to the warping of the HCS as seen in CR 1912 and centred on $\phi_0 = 255°$. The latitudinal excursions of the HCS are further enhanced in the subsequent rotations with the increases in the non-axisymmetric field (see Figure 1b). We have labelled on Figure 3 the most pronounced isolated and polar coronal hole extensions occurring at low latitudes. A CH reoccurring at the same longitude is given the same letter. Two prominent CHs recur during these six rotations, namely, D and E. The emergence of the active region has led to the formation in CR 1913 of the northern polar coronal extension labelled D. The increases of the northern polar coronal hole size east of the HCS warp (*i.e.*, at lower ϕ_0) will be relevant to our later analysis and are indicated by the letters A, B, C, F, and G.

The occurrence of CHs in the low-latitude regions changes the topological distribution of open field lines. Wang and Sheeley (1990) have demonstrated that an empirical relation exists between the rate of flux tube expansion from the photosphere to $2.5 R_\odot$ and the solar wind speed streaming out from that flux tube. The more a flux tube expands, the slower the out-streaming wind becomes. More low-latitude open field lines gathering around active regions increase the chance that fast and slow flow coexist at adjacent longitudes, thereby leading to gradients in solar wind speed (CIRs) in the interplanetary medium.

Figure 4 shows the difference, ΔV, between solar wind speed (V) values separated by 36 hours as measured at Earth by the IMP 8 satellite and plotted here as a function of CR number and Carrington longitude at Earth, ϕ_1. The largest speed gradients on this plot

(shown in red) can all be assigned to the leading edge of one of the prominent CHs of Figure 3 if one allows for a 4 – 5 days transit time from the corona ($r = 2.5R_{\odot}$) to Earth ($r = 1$ AU) corresponding to a Carrington longitude difference ($\phi_0 - \phi_1$) of 40° – 50°.

The various speed gradient increases, as well as their shifts in time of occurrence, can be explained by the morphology and movements of CHs seen in Figure 3. CH D is more prominent during CRs 1913, 1914, and 1915 than during CR 1912 or 1916 – 1917. The recurring wind speed enhancement D (Figure 4) has shifted to higher longitude between 1914 and 1915; this is seen in the change of CH D position from CR 1914 to CR 1915 to slightly larger ϕ_0. CH E, however, is largest in CRs 1914 and 1915 and this is seen as an associated peak speed gradient value during these rotations. The shift in the time of occurrence of the speed enhancement E is not clearly visible in Figure 3 but is, as we shall see, well explained by numerical modelling of the interplanetary medium. CH E is a southern polar coronal hole extension that formed towards the negative pole of the bipolar region and CH D was a northern polar coronal hole extension formed towards the positive pole of that same active region. The reader is referred to Wang, Hawley, and Sheeley (1996) for a theoretical explanation of this phenomenon. The fast wind attributed to features A, B, C, and F are due to warps in the polar hole boundaries, which are clearly seen in the NSO red curve and to a lesser extent in the MDI images. These warps bring high-speed wind into the ecliptic, forcing the enhancements seen at Earth. In the following numerical modelling, we will refer to the polar coronal hole boundary shifts A and F as NPH 1 and C and G as NPH 2.

Comparing Figures 2 and 4 directly, we can see that GCRs start decreasing following passage of the speed gradients induced by CH E and at Earth ($\phi_1 \sim 180°$). CH D was the most visible feature at the time owing to our position north of the ecliptic, yet Figures 2 and 4 show it caused no coherent decrease in GCRs: Rather it is associated with a large increase in GCRs (red region). The large enhancement in the size of CH E, along with the associated large increase in speed gradient, is correlated with the largest and longest decrease in cosmic rays. As found by Bromage, Browning, and Clegg, the cosmic-ray decrease is correlated with a disruption of the streamer belt. We here have shown that another coronal hole (less visible than D in the northern hemisphere) appears to be the cause of that disruption.

From this analysis, it is readily seen that inspection of in-ecliptic solar wind speed V does not explain why GCRs responded to the occurrence of CH E (south of the HCS) but not CH D (north of the HCS). The large ecliptic speed gradients and their associated local **B** field magnitude increases (and increased turbulence) tend to mark times of large GCR changes, but they do not lead systematically to long-lived and consistent GCR decreases. Hence one cannot associate all CHs with subsequent GCR decreases. In the next section, we investigate why some CIRs cause GCR flux decreases while others do not.

4. The Latitudinal Extent of CIRs as a Controlling Mechanism

A long-term GCR decrease (meaning here $>3-4$ days) can only occur in the interplanetary medium if the decrease caused by the disrupted magnetic field ahead of the transient outweighs the recovery process (Wibberenz *et al.*, 1998). The way that GCRs recover after the passage of an interplanetary transient is currently thought to be dictated by two processes: diffusion and the large-scale pattern of GCR flows regulated by gradient and curvature drift motions. The CIRs analysed here all occurred for the same drift-induced GCR flow pattern where protons are believed to stream from high to low latitudes. (By convention the solar magnetic field is said to have an $A > 0$ polarity.) The CIR's effect on GCRs is therefore

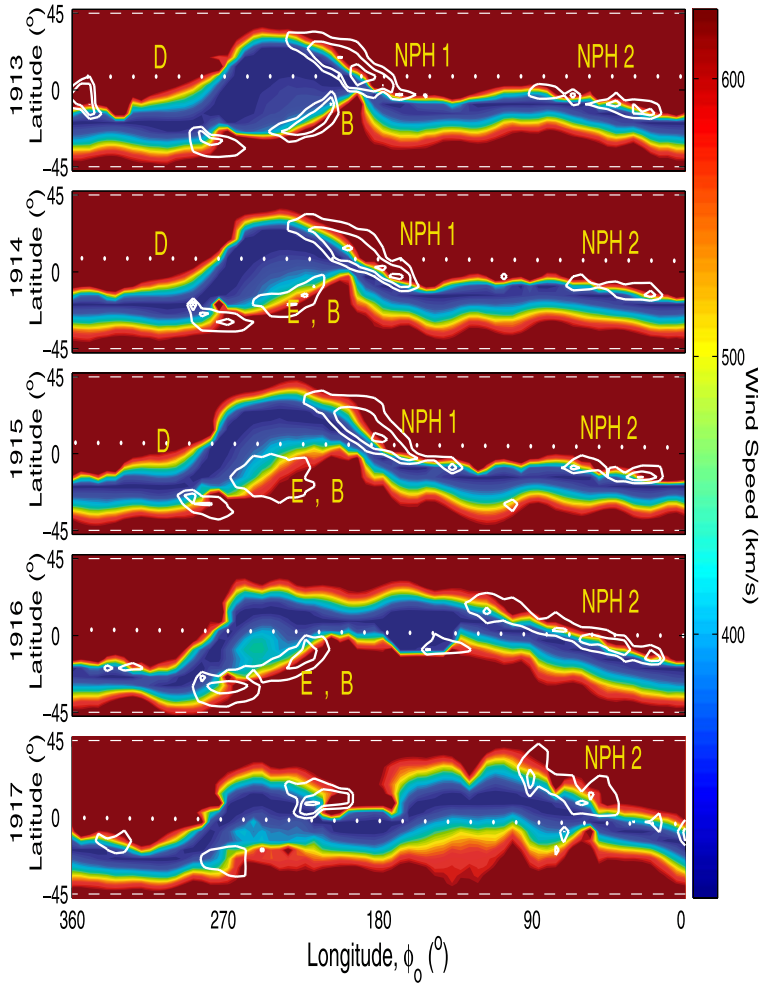

Figure 5 The solar wind speed values predicted by the potential field source surface method are plotted here as a latitude versus time plot. The major CHs identified in Figure 3 are labelled as well as the shifts in polar coronal hole boundaries labelled NPH 1 and NPH 2. This PFSS extrapolation is a smooth prediction (WSO magnetograms have a 5° resolution) of the solar wind speed. Various features seen in the EIT images and the measured 1 AU wind speed are lost. Isocontours (50, 100, 200, and 400 km s^{-1}) of the positive temporal speed changes over 40 hours are indicated by white lines.

more likely to be related to variations in the diffusion mechanisms. In turn these features are related to the CIR topology, the way the magnetic field is gathered in all spatial directions, and the fluctuations forced by the turbulent flows inside the CIR.

The axisymmetric nature of CIRs naturally leads us to investigate changes in the latitudinal dimension. The Wang and Sheeley empirical law allows predictions of the solar wind speed variations for all latitudes and longitudes at the source surface ($2.5 R_{\odot}$). Figure 5 shows the PFSS predictions of the solar wind speed at the source surface for CR 1913 to 1917. These predictions are obtained from calculated flux tube expansion factors and are again plotted for each rotation in a $\sin(\psi)$ versus ϕ_0 format. An expansion factor is obtained

by evaluating the ratio of the areas covered by a given flux tube at the source surface to that on the photosphere (Wang *et al.*, 1997b). Each expansion factor yields a solar wind speed value. The fast flow is shown in dark red and the slow flow in dark blue. The expected positive temporal speed gradients induced by solar rotation are indicated by white isocontour lines for four gradients (50, 100, 200, and 400 km s^{-1}) per 40 hours. Only positive gradients are shown because they reveal fast flow following slow flow at a given ψ, which can lead to formation of an interaction region. This PFSS prediction has a resolution of 8 hours in longitude and also represents an idealisation of the 3-D distribution of V. The largely diverging flux tubes on the boundaries of coronal holes are usually adjacent to the streamer belt and tend to emit slow flows as revealed here. Large concentrations of open field lines, unable to diverge similarly, are associated with fast flows, so that the largest CHs seen in Figure 3 appear in Figure 5 as expansions of fast flow regions towards the ecliptic. The presence of CHs B, D, E, NPH 1, and NPH 2 are discernable and identified on these plots. The effect of CHs B and E have merged into a large southern region of fast flow (labelled B and E).

The largest and most latitudinally extensive solar wind speed gradients, in CR 1913 to 1916, are caused by, respectively, the southern CHs B, E and the slowly expanding flux tubes of the northern polar coronal hole (NPH 1). Both large gradients are extending towards the ecliptic around $\phi_0 = 230°$ in CR 1913. The intersection of these gradients with the Earth's orbit (dotted white points) led to the wind speed enhancements signatures at $\phi_1 = 190°$ and $\phi_1 = 140°$ in Figure 4. The PFSS method failed to predict the ecliptic speed gradient seen in Figure 4 forced by the Elephant Trunk (CH D) other than for CR 1913 (for which it is seen at $\phi_0 \approx 360°$ and $-20° < \psi < 5°$). This is probably due to the resolution of the magnetograms. The slow flow ahead of the Elephant Trunk (CH D) is very limited in latitude (flat streamer belt) and small out-of-ecliptic excursions have been averaged out by the PFSS extrapolation. The same is true for CH C (now merged with G in the structure NPH 2), which caused a speed gradient at Earth, as seen in Figure 4. As we shall see, extrapolation of higher resolution magnetograms predict the occurrence of these latitudinally limited CIRs. Nevertheless, Figure 5 provides an explanation for the substantial GCR decrease following passage of the CIR E. The fast wind emitted by CH E appeared at the times and longitudes of the large warping of the HCS triggered by the emergence of the bipolar region. This topology was favourable for the formation of a CIR with a large latitudinal extent (ψ extending from near $-45°$ to close to the solar equator). GCRs scattered by the compressed IMF cannot replenish the depleted regions easily as they are forced to propagate around a larger structure. The scattering then outweighs the recovery process.

The solar wind speed predictions were extended to the interplanetary medium by using the ENLIL 3-D MHD numerical model of the solar wind (Odstrcil and Pizzo, 1999a, 1999b). The Community Coordinated Modelling Center (CCMC) Web-based interface was used for the run. The numerical code is based on a flux-corrected algorithm that extends the source surface prediction of the solar wind speed and magnetic field polarity to the interplanetary medium. CR 1913 to CR 1915 were simulated by using the source surface wind speed predictions based on smoothed and filtered magnetograms of the National Solar Observatory at Kitt Peak (with preparation of these magnetograms carried out by Dr. N. Arge). The source surface model constructs a spherical harmonic representation, and before doing this it interpolates the NSO 1° resolution magnetograms onto a grid with 2.5° resolution. So the effective resolution of the MHD predictions based on the PFSS model and Kitt Peak data (*i.e.*, the PFSS – ENLIL combination) is also about 2.5°. The outputs of the numerical code are the magnetic field vector, solar wind velocity vector, and plasma number density over the heliocentric distance (r) range from 0.1 to 2.3 AU. The left-hand side of the figure shows the normalised magnetic field intensity from 0.1 to 2.3 AU in the solar ecliptic plane.

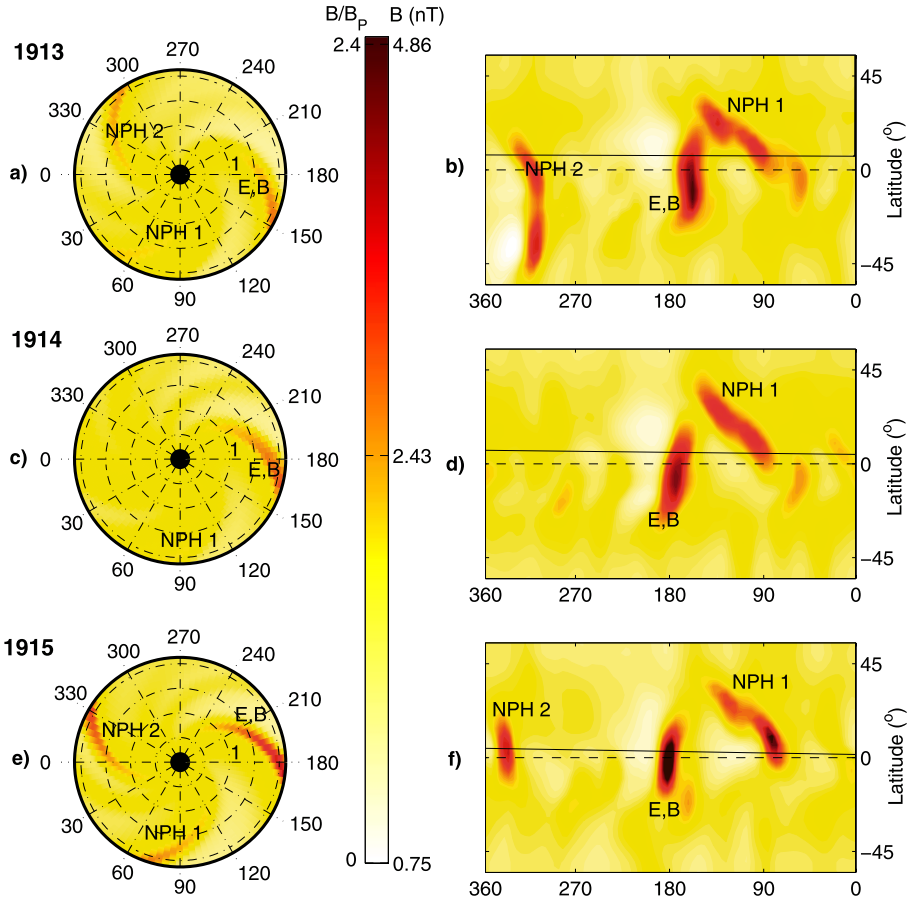

Figure 6 The MHD predictions made using the ENLIL numerical code for CRs 1913 – 1915. The effect of C, the combined effect of E, B, and that of NPH discussed on the source surface plot (Figure 5) are seen as CIRs in the left-hand plots of the in-ecliptic normalised B field magnitude prediction (panels a, c, and e) where the longitude scale refers to $\phi_0(^\circ)$ at $r = 2.5R_\odot$. In the right-hand plots of latitude versus longitude absolute B field value predictions are at $r = 2$ AU, and longitude also refers to the longitude at $r = 2.5R_\odot$ (panels b, d, and f) for easy comparison. The normalised B field values of panels a, c, and e were obtained by taking the ratio with the value predicted by Parker spiral theory, B_P.

The normalisation is obtained by dividing the simulated values of B by the expected Parker spiral field strength (B_P in the case of no compression). The compression regions associated with the various CHs shown in Figure 3 (and identified in Figure 5) are labelled on the six panels of Figure 6.

The in-ecliptic IMF enhancement (at Earth's latitude) at Carrington longitude $\phi_2 = 170^\circ$ (at $r = 2$ AU) during CR 1913 is the CIR associated with CHs E and B. (Note that this is at $\phi_1 = 220^\circ$ at $r = 1$ AU and $\phi_0 = 250^\circ$ at $r = 2.5R_\odot$.) The growth in size of CHs NPH 2 (C in Figure 3) and E during CR 1915 is marked here by an enhancement of the corresponding CIR's magnetic field compression. The right-hand side of the plot (panels d, e, and f) displays latitude – longitude (ψ, ϕ_2) plots of the unnormalised compressed magnetic field magnitude (in nanoteslas) at $r = 2$ AU. The three in-ecliptic CIRs predicted by ENLIL seen in panels a, b, and c also dominate in panels d, e, and f. Various features can be recognised,

such as the earlier formation of the CIR associated with CHs E and B. Inspection of Figure 4 reveals that the speed gradient associated with E shifted from $\phi_1 = 200°$ to $\phi_1 = 230°$ between CR 1914 and CR 1915. These shifts were induced by the rapid growth of CH E between these two rotations, as seen clearly in Figure 3 (green band) and seen in the variation of the non-axisymmetric open flux, which is enhanced between CR 1914 and CR 1915 (see Figure 1b).

The predicted IMF enhancement also intensified during the interval from CR 1913 to CR 1915 for CIR E, B, but the latitudinal extent of the structure remained very similar. The latter observation is expected because the latitudinal excursion of the HCS remains constant. CR 1915 is marked by a longer lived GCR decrease than for CR 1913 or CR 1914 (see Figure 2). This is therefore not explained by the latitudinal extent of the interaction region alone. GCRs only recover during the start of the next rotation, which suggests that the presence of the third kinematic steepening and CIR formation (NPH 2 in CR 1915) also prevents GCRs from recovering. CIR NPH 2 has a detectable effect on GCRs during CRs 1912, 1913, and 1915, seen in Figure 1 as a decrease at the onset of these three rotations. Finally, we note that the effect of CIR NPH 2 with the enhanced effect of the structures B, E, and NPH 1 leads to the double-peaked GCR structure for these rotations. The ENLIL predictions show that CIR C disappears during CR 1914 and the double-peaked structure in GCRs accordingly disappears during that rotation.

The morphology of CIRs and their effect on GCRs are now inspected in more detail.

5. Response of the HCS to Enhanced Low-Latitude Open Field and Effect on GCRs

The interaction of fast and slow flow in the heliosphere leads to the formation of stream interfaces where the flows cannot mix (the "frozen-in" condition applies) and both are largely deflected. Azimuthal flow deflections up to 6° in interaction regions have been observed at 1 AU: these are westward in the shocked slow stream and eastward in the shocked fast stream. The same effect in latitude has been detected by *Ulysses* near 4 – 5 AU (Gosling *et al.*, 1978). The meridional flow deflections observed by *Ulysses* in the northern hemisphere can be as large as 8° and are southward (northward) in the shocked slow (fast) streams, with opposite deflections in the southern hemisphere (Gosling *et al.*, 1997; Riley *et al.*, 1996; Gosling and Pizzo, 1999).

We now compare the GCR step decreases during CR 1915 to the evolution of the CIR morphology as it crosses 1 AU. Forman and Gleeson (1975) showed that GCRs corotate with the Parker spirals of the solar wind. At 1 AU this represents a speed of order ∼400 km s^{-1} in the same direction as the Earth's orbital motion (30 km s^{-1}). Thus structure in cosmic-ray fluxes associated with CIRs overtakes the Earth from the direction of 18 hours local time (Hall, Duldig, and Humble, 1996). Later models by Levy (1976) and Erdős and Kóta (1979) refined this Forman – Gleeson model by including drifts and showed that the arrival direction of the anisotropy is also affected by drifts shifting from 18 hours local time during $A < 0$ polarity to 15 hours local time for the $A > 0$ polarity. The study of GCR variations on resolution of several days requires removal of these diurnal variations recorded by neutron monitors.

We here remove the diurnal variation by using two neutron monitors with the same rigidity cutoff on opposite sides of the Earth. The 24-NM-64 Novosibirsk neutron monitor in Russia is located at geographic latitude $\lambda_{\text{Earth}} = 54.80°$, geographic longitude $\phi_{\text{Earth}} = 83.00°$, and altitude $h = 163$ m and has a cutoff rigidity of $R_C = 2.69$ GV. The 9-NM-64 Newark neutron monitor (USA), at $\lambda_{\text{Earth}} = 39.68°$, $\phi_{\text{Earth}} = 284.25°$, and altitude $h = 50$ m, has a

cutoff rigidity of 2.21 GV. Thus these two neutron monitors, separated by $\Delta\phi_{\rm Earth} = 201.25°$, have similar rigidity cutoffs and altitude. Their low altitude means that they are not as sensitive as Climax (*i.e.*, have lower count rates); however, their unique spatial distribution (same rigidity cutoff and location on opposite sides of the Earth) allows removal of the solar diurnal variation. The 24-hour running means of the Newark neutron counts ($\rm NE_{Fit}$) were fitted to the 24-hour running means of those at Novosibirsk (NO). The mean $[(\rm NE_{Fit} + NO)/2]$ was taken and is plotted in Figure 7a. The interplanetary conditions (near $r = 1$ AU in the ecliptic plane) during this GCR decrease are also plotted. Figures 7b and g show the $V_y|_{\rm GSE}$ and $V_z|_{\rm GSE}$ components of the solar wind speed in Geocentric Solar Ecliptic (GSE) coordinates of the solar wind velocity vector from the OMNI-tape data set. The magnitude of the velocity (dominated by $V_x|_{\rm GSE}$) is plotted in Figure 7c in two colours: blue for $B_x|_{\rm GSE} < 0$ (outward field; *i.e.*, an away sector) and red for $B_x|_{\rm GSE} > 0$ (inward field; *i.e.*, toward sector). The IMF strength is plotted in Figure 7e. The ENLIL MHD predictions of the solar wind speed, IMF strength, and latitudinal deflection of the flows are also plotted in Figures 7d, f, and h, respectively, for this period and for a latitude range of $\psi \in [-55° : 55°]$. The orbit of the Earth in the coordinate system used by ENLIL is shown by a quasi-horizontal black line near 4.5° north of the solar equatorial plane.

The OMNI data show two noticeable solar wind speed increases during the period at $t = 1996.822$ and $t = 1996.842$ (Figure 7c). The former is the larger of the two and is associated with the southern, inward field coronal hole (CH E of Figure 3) clearly visible in the ENLIL simulation in Figure 7d. The GCR variations (Figure 7a) show two main step decreases between $t = 1996.82$ and $t = 1996.85$ and a minor one at time $t = 1996.84$. The onsets of these decreases were marked by vertical line crossing the entire figure. It is apparent that only one of the two visible CIRs in the ecliptic is associated with one of the two large GCR decreases (the first one). This first GCR decrease occurred close to the HCS passage across the ecliptic at the front of the CIR associated with CH E. The second main GCR decrease, however, occurs on the trailing edge of that CIR when a GCR increase is usually observed (*i.e.*, in the less turbulent rarefaction region). The third, less important, GCR decrease is associated with the arrival of the second CIR seen in Figure 7b. We note that all three GCR decreases occur around the onset of IMF strength increases (Figure 7e) and in proximity of stream interfaces. In particular, the latitudinal deflection of the flow (Figure 7g) reverses systematically close to these decreases.

The occurrence of GCR decreases resulting from IMF enhancements is traditionally modelled in the heliosphere by the CR – B relation of Burlaga, Ness, and McDonald (1995). In this relation, the IMF strength controls the GCR decrease by reducing the diffusion coefficient. Inspection of Figure 7e shows that the increase in the IMF associated with the second major GCR decrease is much smaller than the IMF increases during the first and third decrease. The third decrease in GCR is very small compared to the in-ecliptic IMF enhancement. The second GCR flux decrease is very puzzling as it is not associated with a clear solar wind speed or magnetic field enhancement at Earth.

This latter anomaly can be understood by considering the latitudinal distribution of solar wind flow gradients, their associated latitudinal deflections, and the compressed B fields shown in Figures 7f and h. Figure 7f shows that the shift in fast wind occurrence induced by the stretching of the warp in the HCS has led to three distinct and widely separated B field compressions around ($t = 1996.821, \psi = -10°$), ($t = 1996.835, \psi = 20°$), and ($t = 1996.842, \psi = 10°$). The GCR decreases are here systematically followed by southward deflections of the flows at Earth (Figures 7g and h). This can be understood from Figure 7h. The first decrease is followed by fast wind deflected at the stream interface southward (from CH E) owing to a negative slope in the HCS warp. The second GCR decrease

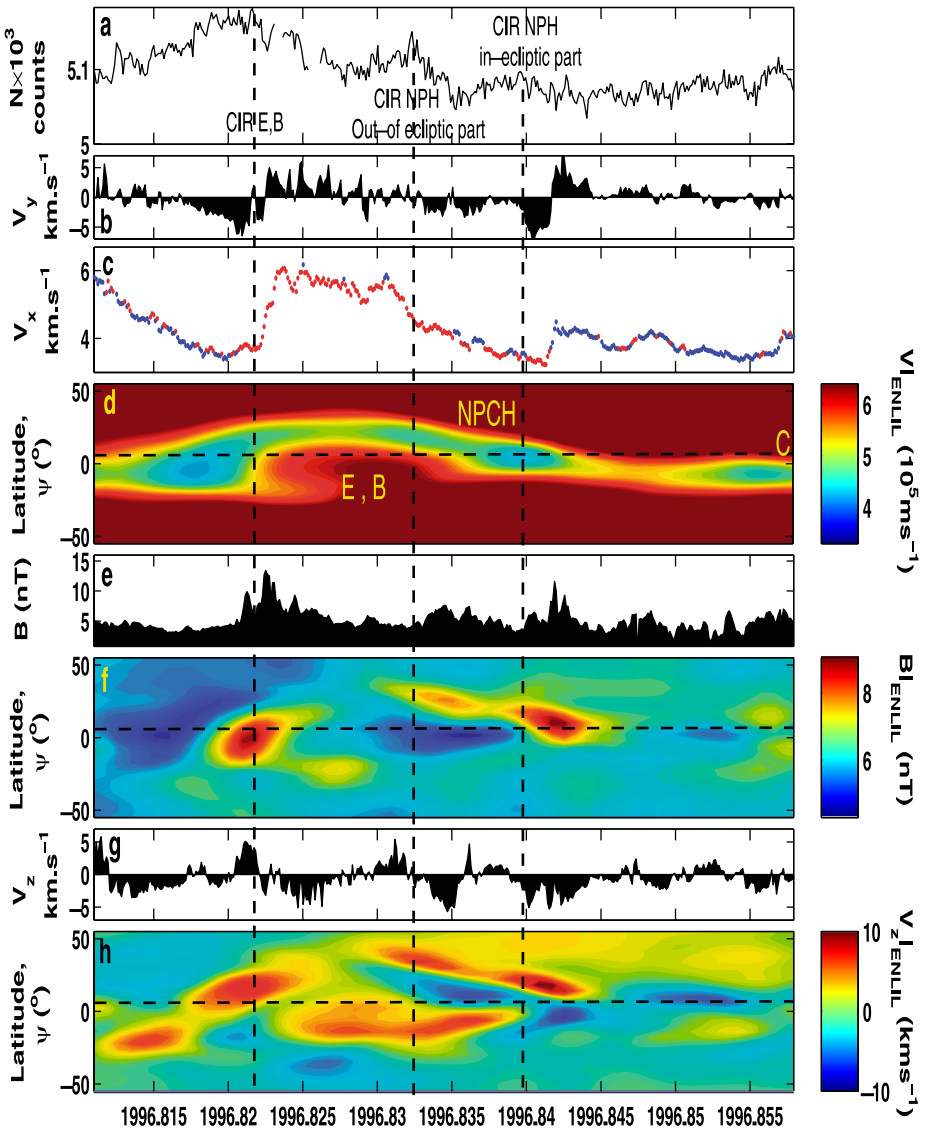

Figure 7 A summary of the data during CR 1915. (a) The GCR variation after removal of the solar diurnal anisotropy. (b) V_y (tangential) component of the speed flow in the GSE frame at 1 AU measured by IMP 8. (c) V_x (radial) component of the speed flow at 1 AU measured by IMP 8. (d) The solar wind speed at $r = 1$ AU, predicted by the ENLIL code, $V|_{\mathrm{ENLIL}}$, plotted as a function of latitude Ψ and time. (e) The magnitude of the IMF, **B**, at 1 AU measured by IMP 8. (f) The IMF strength at 1 AU predicted by the ENLIL code, $B|_{\mathrm{ENLIL}}$, in the same format as panel d. (g) V_z component of the speed flow in the GSE frame at 1 AU measured by IMP 8. (h) The ENLIL prediction of the latitudinal perturbation to the CIR flow in the same format as panel (d). The vertical dotted lines mark the times of GCR decrease onsets, as shown in panel a (also seen in Figure 1a).

occurs during the southern deflection of the slow solar wind ahead of the higher latitude CIR (positive slope in the HCS warp). The third decrease is also followed by slow flow deflected by the third speed enhancement (which has a positive slope). Hence this analysis provides evidence that decreases seen in GCRs at Earth can be remotely connected to CIRs compressing the magnetic field at higher latitude. In this case the fast flows emitted in the low-latitude region by the northern polar coronal extension NPH 1 cause the magnetic field to be mainly compressed at high latitudes not sampled by the Earth. The inability of GCRs to recover before the third decrease (the in-ecliptic part of the CIR induced by NPH 1) shows that the CIR responsible for the second decrease has a lasting effect.

6. Discussion

The mere occurrence of a polar coronal hole extension in the vicinity of the ecliptic plane does not necessarily lead to a decrease in cosmic rays. Comparison of Figures 2, 3, and 4 shows that the reverse can occur when the IMF emerging from the coronal hole consists mostly of a latitudinally limited and weakly compressed field in the interplanetary medium.

The use of the PFSS method and MHD numerical simulations of the IMF in Figures 5 and 6 shows that a GCR decrease only occurred if the streamer belt warped such that fast flow followed slow flow over a wide latitude range. The three large latitudinally extensive CIRs of CR 1913 and CR 1915 have clear imprints on GCRs and, from this comparison, the shape of the original time series of GCR fluxes can be explained (Figure 1). The presence of a warped HCS leads to compressed IMF that extends over a wide latitude range. Evidence has been presented here that it is this feature that prevents the GCR flux from recovering.

Traditionally CIRs are thought to cause GCR decreases at Earth when the large structure passes over the Earth. However, the occurrence of a GCR decrease on the trailing edge of a CIR (when no speed increase and a very weak IMF increase were observed) cannot be accounted for unless one considers large IMF increases occurring at higher latitudes. In particular, the step decreases in GCR flux during CR 1915 occur systematically during the in- or out-of-ecliptic 1 AU passage of compressed IMF. These findings have important implications for our understanding of the diffusion of GCRs in the interplanetary medium. The diffusion of GCRs is usually separated into two components: along (parallel) and across (perpendicular) the magnetic field lines. GCR random walk was, until recently, thought to be very small across magnetic field lines. The *Ulysses* mission showed that recurrent energetic particle events could be seen at very high latitudes with no clear CIR plasma nor magnetic signatures present (Kunow, Heber, and Simpson, 1998). This remote connection of GCRs to lower latitudes was associated with two different processes, a non-Parkerian IMF (Fisk, 1996) or a higher cross-field line diffusion, $\kappa_{\perp}$ (Kóta and Jokipii, 1995). The non-Parkerian field lines are drawn in by the large latitudinal circulation of open field lines below the source surface and are thought to extend from the polar region to latitudes as low as 30°. The response of GCRs reported here is at Earth and yet is to structures at latitudes of 30° and below where the Fisk circulation is not as prominent. Hence the effect of a large $\kappa_{\perp}$, as predicted by Kóta and Jokipii, could be the required explanation in this case. Hence the event analysed in this paper suggests that the decrease originally caused at higher latitude is communicated to lower latitudes by the ability of GCRs to cross the Archimedian spirals.

7. Concluding Remarks

Various features of the effect of coronal holes on the dynamics of GCRs have been studied in this paper. Evidence has been presented that the latitudinal extension of CIRs is a controlling factor for GCR shielding. The combined effect of CIRs covering 50° of latitude and separated by 3 – 4 days forced a long GCR decrease during CRs around 1915. The second CIR (at higher latitude) began to have a large effect on GCRs before its arrival at Earth. The GCR decrease occurred during the in-ecliptic passage of the trailing fast wind of the first CIR induced by the fast flows of the southern isolated coronal hole. We associate the GCR decrease in the rarefaction region to out-of-ecliptic IMF compressed by a CIR mainly formed by the warping of the HCS at higher latitude. This implies that the source of the GCR decrease was a large IMF compression occurring at higher latitudes that the Earth only partly intersected.

Acknowledgements The referee is thanked for suggesting the use of NSO/Kitt Peak synoptic maps. The NSO/Kitt Peak data used here are produced cooperatively by NSF/NOAO, NASA/GSFC, and NOAA/SEL. We thank Yi-Ming Wang of the Naval Research Laboratory for providing the PFSS data, Ms. Anna Chulaki of the Community Coordinated Modelling Center (CCMC) for helpful information, running the MHD ENLIL code, and providing a great service. The MHD code run at the CCMC was written and is regularly updated by Dr. D. Ostrcil and Dr. N. Arge. We also thank Dr. B.S. Lanchester for continuous support. This work was funded by the National Environment Research Council (NERC, UK) and the Particle Physics and Astronomy Research Council (PPARC, UK). The Synoptic EIT images were provided by Dr. Benevolenskaya. The cosmic-ray data were provided by the Space Physics Data System, University of New Hampshire, for Climax (P.I.: Dr. C. Lopate); the Bartol Research Institute, University of Delaware, for Newark (P.I.: Prof. J.W. Bieber), and the Russian Academy of Sciences Solar-Terrestrial Division of Izmiran for Novosibirsk. The OMNI-2 interplanetary magnetic and solar wind flow data were compiled by the NASA/Goddard Space Flight Center, Space Physics data facility, and distributed by the World Data Center, CCLRC, Chilton, UK.

References

Benevolenskaya, E.E., Kosovichev, A.G., Scherrer, P.H.: 2001, *Astrophys. J.* **554**, L107.
Bromage, B.J.I., Browning, P.K., Clegg, J.R.: 2001, *Space Sci. Rev.* **97**(1/4), 13.
Burlaga, L.F., Ness, N.F., McDonald, F.B.: 1995, *J. Geophys. Res.* **100**(A8), 14763.
Cliver, E.W., Ling, A.G.: 2001, *Astrophys. J.* **556**, 432.
Erdős, G., Kóta, J.: 1979, *Proc. 16th ICRC* **4**, 45.
Fisk, L.: 1996, *J. Geophys. Res.* **101**, 15547.
Fisk, L., Schwadron, N.A.: 2001, *Space Sci. Rev.* **560**, 425.
Forman, M.A., Gleeson, L.J.: 1975, *Astrophys. Space Sci.* **32**, 77.
Gosling, J.T., Pizzo, V.J.: 1999, *Space Sci. Rev.* **89**, 21.
Gosling, J.T., Asbridge, J.R., Bame, S.J., Feldman, W.C.: 1978, *J. Geophys. Res.* **83**, 1401.
Gosling, J.T., Bame, S.J., Feldman, W.C., McComas, D.J., Riley, P., Goldstein, B.E., Neugebauer, M.: 1997, *J. Geophys. Res.* **24**, 309.
Hall, D.L., Duldig, M.L., Humble, J.E.: 1996, *Space Sci. Rev.* **78**, 401.
Harvey, K.L., Recely, F.: 2002, *Solar Phys.* **211**, 31.
Heber, B., Burger, R.A.: 1999, *Space Sci. Rev.* **89**, 125.
Kóta, J.: 1999, *Space Sci. Rev.* **89**, 311.
Kóta, J., Jokipii, J.R.: 1991, *Geophys. Res. Lett.* **18**, 1797.
Kóta, J., Jokipii, J.R.: 1995, *Science* **268**, 1024.
Kunow, H., Heber, B., Simpson, J.A.: 1998, *Space Sci. Rev.* **83**, 215.
Lee, M.: 2001, *J. Geophys. Res.* **105**, 10491.
Levy, M.: 1976, *J. Geophys. Res.* **18**, 2082.
Morfill, G., Richter, A.K., Scholer, M.: 1979, *J. Geophys. Res.* **84**, 1505.
Odstrcil, D., Pizzo, V.J.: 1999a, *J. Geophys. Res.* **104**, 483.
Odstrcil, D., Pizzo, V.J.: 1999b, *J. Geophys. Res.* **104**, 493.
Pizzo, V.J., Gosling, J.T.: 1994, *Geophys. Res. Lett.* **25**, 1529.

Riley, P., Gosling, J.T., Weiss, L.A., Pizzo, V.J.: 1996, *J. Geophys. Res.* **101**, 24349.
Rouillard, A.P.: 2007, Ph.D. thesis, Space Environment Physics Group, University of Southampton, UK.
Wang, Y.M., Sheeley, N.R.: 1990, *Astrophys. J.* **355**, 726.
Wang, Y.M., Hawley, S.H., Sheeley, N.R.: 1996, *Science* **271**, 464.
Wang, Y.M., Sheeley, N.R. Jr., Howard, R.A., Kraemer, J.R., Rich, N.B., Andrews, M.D., Brueckner, G.E., Dere, K.P., Koomen, M.J., Korendyke, C.M.: 1997a, *Astrophys. J.* **485**, 875.
Wang, Y.M., Sheeley, N.R., Phillips, J.L., Goldstein, B.E.: 1997b, *Astrophys. J.* **488**, L51.
Wang, Y.M., Sheeley, N.R., Rouillard, A.P.: 2006, *Astrophys. J.* **644**, 638.
Wibberenz, G., Le Roux, J.A., Potgieter, M., Bieber, J.W.: 1998, *Space Sci. Rev.* **83**, 309.